Modeling creeping flows in porous media using regularized Stokeslets

Suraj Kumar Kamarapu, Mehdi Jabbarzadeh, and Henry Chien Fu*
Department of Mechanical Engineering, University of Utah, Salt Lake City, Utah 84112, USA

(Received 7 January 2022; accepted 2 September 2022; published 24 October 2022)

Flows in porous media in the low-Reynolds number regime are often modeled by the Brinkman equations. Analytical solutions to these equations are limited to standard geometries. Finite volume or element schemes can be used in more complicated geometries, but become cumbersome when there are moving boundaries that require frequent remeshing of the domain. In Newtonian fluids, the method of regularized Stokeslets has gained popularity due to its ease of implementation, including for moving boundaries, especially for swimming and pumping problems. While the corresponding method of regularized Brinkmanlets can be used in a domain consisting entirely of Brinkman medium, many applications would benefit from an easily implemented representation of flow in a domain with heterogeneous regions of Brinkman medium and Newtonian fluid. In this paper, we model flows in porous media by placing many static regularized Stokeslets randomly in three dimensions to emulate the forces exerted by the rigid porous structure. We perform numerical experiments to deduce the correspondence between the chosen density and blob size of regularized Stokeslets in our model, and a Brinkman medium. We demonstrate our model for two scenarios of microswimmers near porous media.

DOI: 10.1103/PhysRevFluids.7.104102

I. INTRODUCTION

Flow through porous media is encountered in many natural and industrial systems [1]. A quantitative description of flows in porous media is extremely important for understanding flow phenomena or designing such systems. Mathematical modeling of such flows has been an active area of research in many fields, including, but not limited to, medicine [2], fluid mechanics [3], hydrology [4], geophysics [5], and soil mechanics [6]. A volume-averaged description of flow parameters and global description of porous structure (e.g., porosity, permeability) helps avoid the characterization of spatially intricate flows through small-scale porous structures. Attempts to derive equations describing flows through porous media date back to 1856 when Darcy [7] reported empirical relations based on experimental observations relating the averaged fluid velocity to the pressure drop via a linear relationship. This model presumes that the averaged flow field is uniform in the domain and the drag offered by the porous structure dominates viscous shear forces in the fluid. It fails to model flows in a highly porous domain and near boundaries [8]. For nonuniform flows through porous media, the Brinkman equation was proposed in 1949 [9] to describe flows past a dense swarm of static spherical particles. Here, the viscous forces due to velocity gradients in the fluid flow become comparable to the drag force exerted by the porous structure leading to the Brinkman equations [9],

$$-\nabla p = -\mu\nabla^2\mathbf{u} + \mu\alpha^2\mathbf{u}, \quad \nabla\cdot\mathbf{u} = 0, \tag{1}$$

*henry.fu@utah.edu

where p is the averaged pressure, $\mathbf{u}$ is the averaged fluid velocity, and μ is an effective viscosity. Various theoretical studies have shown that this model accurately describes the flow in dilute porous media [8,10–15]. In this dilute limit, the effective viscosity is related to the viscosity of the fluid phase alone (μ_0) by $\mu = \mu_0/\phi$, where ϕ is the porosity (volume fraction of fluid) in the medium [16]. The parameter α is called the resistance of the porous medium and, in the limit $\phi \to 1$, α^{-2} is the permeability of the medium. The value of α sets the length scale (α^{-1}), called the Brinkman screening length, over which the fluid flow decays in a given porous medium. In the absence of porous structure in the fluid flow, $\alpha \to 0$ and the Brinkman equation reduces to the Stokes equation ($-\nabla p + \mu \nabla^2 \mathbf{u} = 0$).

The Brinkman equation has been used in a variety of applications to mathematically model flows through undeformed gels [17], arrays of fixed fibers [18], blood clots [19], and particles in a microfluidic channel [20], as well as how porous media damp flows [21], and confine active swimmers [22–24]. Analytical solutions for the flows obeying Brinkman equations can be derived for problems involving simple geometries such as two-dimensional waving sheets, spheres, or cylinders [22,23,25,26], but they are generally not available for flows involving complicated geometries. For domains of arbitrary shapes, numerical solutions can be obtained via finite volume or element schemes, for which the resolution of the discretization dictates the accuracy and computational cost of these numerical solutions. Implementation of these schemes becomes cumbersome when there are moving boundaries, such as the surface of a swimming bacterium, as it requires frequent remeshing of the domain. If the medium around the moving boundary is a homogeneous Brinkman medium, the method of regularized Brinkmanlets is quite useful [27,28], and Green's functions for anisotropic but spatially homogeneous permeability are also available [29]. However, these Green's function based approaches are not valid when there is a heterogeneity involved. An example of such a heterogeneous mixture is a porous medium next to a Stokes fluid, as encountered by the bacterium *Helicobacter pylori* swimming in a fluid pocket surrounded by gastric mucus [22,23], or around growing blood clots inside a microfluidic channel [19]. Such heterogeneous domains can be treated using finite volume schemes, but that can become cumbersome as it requires frequent remeshing of the domain and accounting for complicated boundary conditions along the interface of two fluids. Here we present a computational framework to address fluid flows in such situations using regularized Stokeslets.

Our basic approach is to model a porous medium by a random arrangement of many static regularized Stokeslets in three dimensions to emulate a rigid (stationary) porous structure. This is similar in spirit to many past approaches which model flows through porous media as flows around discrete stationary obstacles [12,30–33]. In a heterogeneous domain, only the portion containing the porous medium is represented by a random spatial arrangement of static regularized Stokeslets. In some ways, such a model with discrete obstacles is a more direct representation of a porous medium than the macroscopic continuum Brinkman model, but it is still useful to be able to connect these two models of porous media. The parameter that defines a porous medium via Brinkman equations is the resistance, α. On the other hand, in our proposed model, we define a porous medium using the number density of regularized Stokeslets, ρ, and the blob parameter (size of each regularized Stokeslet), ε. To quantify the relationships between the parameters α and $\{\rho, \varepsilon\}$ in describing the same porous medium, we perform numerical experiments using our proposed model and compare to analytical solutions for the Brinkman model.

This paper is organized as follows: In Sec. II, we review the method of regularized Stokeslets. In Sec. III, we perform numerical experiments involving the proposed model of porous media and match results with the analytical solution obtained using the Brinkman equation. We then connect the input parameters from our model to the resistance of Brinkman medium. In Sec. IV, we apply our model to some example cases of microswimmers moving in heterogeneous scenarios with both fluid and porous medium domains. In Sec. V, we discuss the applicability of the proposed porous medium framework to model flows in porous media.

II. REVIEW OF REGULARIZED STOKESLETS

The method of regularized Stokeslets, introduced in 2001 by Cortez [34], computes the Stokes flow at any point in a domain as the superposition of flow fields generated by forces distributed at material points in a fluid. It uses a Green's function solution, $(\mathbf{u}^\varepsilon, p^\varepsilon)$, of Stokes equations in the presence of a force $(\mathbf{f}^0)$ distributed around position $\mathbf{x}_0$ according to the function $\psi_\varepsilon(\mathbf{x}-\mathbf{x}_0) = \frac{15\varepsilon^4}{8\pi(|\mathbf{x}-\mathbf{x}_0|^2+\varepsilon^2)^{7/2}}$. ψ_ε is a radially symmetric, smooth approximation to a three-dimensional δ distribution with the property that $\int \psi_\varepsilon(\mathbf{x})d\mathbf{x} = 1$, so that $\psi^\varepsilon(\mathbf{x}-\mathbf{x}_0)$ is concentrated near $\mathbf{x} = \mathbf{x}_0$. The approximate size of the distribution is set by the value of the "blob parameter" ε. Thus, $\mathbf{u}^\varepsilon$ and p^ε satisfy

$$-\partial_i p^\varepsilon + \mu\partial^2 u_i^\varepsilon = -f_i^0\psi^\varepsilon, \quad \partial_j u_j^\varepsilon = 0, \tag{2}$$

where p^ε is the pressure, and $\mathbf{u}^\varepsilon$ is the fluid velocity. In this and other equations, we use indicial notation, where $i, j = 1, 2, 3$ denotes Cartesian components and repeated indices are implicitly summed over. The flow field $\mathbf{u}^\varepsilon$ and pressure field p^ε at a point $\mathbf{x}$ are called the regularized Stokeslet and are specified by

$$u_i^\varepsilon(\mathbf{x}) = S_{ij}^\varepsilon(\mathbf{x}-\mathbf{x}_0)f_j^0, \tag{3}$$

$$p^\varepsilon(\mathbf{x}) = P_j^\varepsilon(\mathbf{x}-\mathbf{x}_0)f_j^0, \tag{4}$$

where

$$S_{ij}^\varepsilon(\mathbf{r}) = \frac{1}{8\pi\mu}\left(\frac{\delta_{ij}(r^2+2\varepsilon^2)+r_i r_j}{(r^2+\varepsilon^2)^{3/2}}\right), \tag{5}$$

$$P_j^\varepsilon(\mathbf{r}) = \frac{2r^2+5\varepsilon^2}{8\pi(r^2+\varepsilon^2)^{5/2}}r_j, \tag{6}$$

δ_{ij} is the Kronecker delta, and $r = |\mathbf{r}|$. Crucially, regularizing the point force $(\mathbf{f}^0)$ removes any singularity at $\mathbf{x}_0$, thus simplifying the numerical implementation. The linearity of Stokes equations lets us obtain a solution for multiple forces of the same form, acting at N different locations $\mathbf{x}_q$, for $q = 1, 2, \ldots, N$, by superposition of flow fields generated by each of those forces independently. Thus the flow field $(\mathbf{u})$ and pressure (p) at a point $\mathbf{x}$ are given by

$$u_i(\mathbf{x}) = \sum_{q=1}^{N} S_{ij}^\varepsilon(\mathbf{x}-\mathbf{x}_q)f_j(\mathbf{x}_q), \tag{7}$$

$$p(\mathbf{x}) = \sum_{q=1}^{N} P_j^\varepsilon(\mathbf{x}-\mathbf{x}_q)f_j(\mathbf{x}_q). \tag{8}$$

Representing the flow external to a body using a surface distribution of regularized Stokeslets is an accurate approximation to the representation of the flow via a single-layer representation of the boundary integral equations in the limit of small ε [35]. Our implementation of the method of Regularized Stokeslets for three-dimensional bodies has been previously described [36,37].

Due to the ease of its implementation even in intricate three-dimensional domains, the method of regularized Stokeslets has become a popular choice to numerically model flows governed by the Stokes equations for swimming microorganisms [35,38–40], human sperm [41], flexible filaments [42], microrobots [43–50], tumor tissues [51], micropumps [52–54], phoretic flows [55], and plasma membranes [56]. An interconnected lattice network of regularized Stokeslets has been used to develop a computational framework to represent a viscoelastic fluid [57].

In this paper, we model porous media by filling the domain occupied by porous media with randomly placed regularized Stokeslets, and connect it with a Brinkman equation description of the same medium.

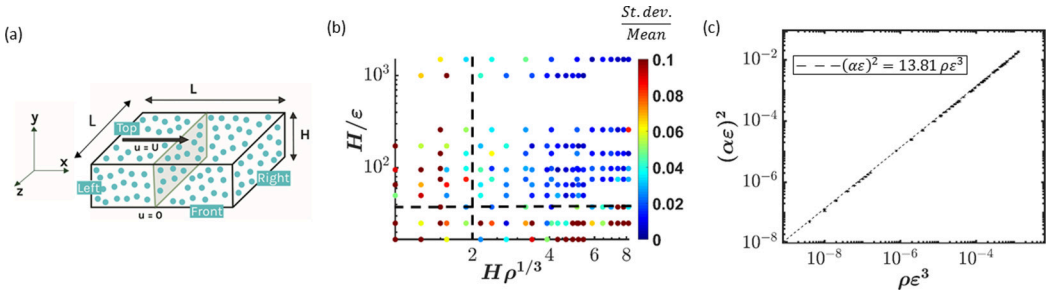

FIG. 1. (a) Box-shaped domain for a portion of the Couette flow driven by the top surface sliding to the right with velocity U. (b) Plot showing the ratio of standard deviation to the mean for estimates of α for a given combination of $\{\rho, \varepsilon\}$, and box height H. (c) Plot showing the dependence of nondimensional Brinkman medium resistance $\alpha\varepsilon$ on nondimensional density $\rho\varepsilon^3$ of regularized Stokeslets. Results are independent of the box height H.

III. NUMERICAL EXPERIMENTS

The parameter that defines a porous medium via Brinkman equations is the resistance, α. On the other hand, in our proposed model, we define a porous medium using the number density per unit volume of regularized Stokeslets (ρ) and the Stokeslet blob parameter (ε). The average spacing between these regularized Stokeslets is given by the length scale $\rho^{-1/3}$. In order to establish a relation between the two models, we perform two numerical experiments using our proposed model and compare to analytical solutions for the Brinkman model to quantify and validate the relationships between α and $\{\rho, \varepsilon\}$. A dimensional analysis suggests that the relationship can be written in the form $\alpha\varepsilon = f(\rho\varepsilon^3, l_1/\varepsilon, l_2/\varepsilon, \dots)$, where the l_i are length scales defining the geometry of an experiment.

A. Couette flow between two plates

In the first experiment, we consider a steady-state flow between two infinitely long plates separated by distance H, filled with a dilute porous medium of resistance α. The top plate moves to the right with velocity U, while the bottom plate is fixed in place.

1. Analytical solution

Following the Brinkman equation, the resistance α can determine the velocity field in the volume bounded by the plates, as shown below. The fluid flow between the plates is governed by the Brinkman equations [Eq. (1)] and must also satisfy the velocity boundary conditions of $\mathbf{u} = U\hat{\mathbf{x}}$ at height $y = H$, and $\mathbf{u} = \mathbf{0}$ at $y = 0$. By symmetry, there is only an x component of the flow which obeys

$$-\frac{\partial p}{\partial x} = -\mu\left(\frac{\partial^2 u_x}{\partial x^2} + \frac{\partial^2 u_x}{\partial y^2} + \frac{\partial^2 u_x}{\partial z^2} - \alpha^2 u_x\right), \tag{9}$$

where u_x is the component of the velocity field in the x direction. The left-hand side of the equation is zero as there is no pressure gradient imposed in the x direction. The first and third terms on the right-hand side are zero by symmetry since $\mathbf{u}$ only depends on y. Solving for the velocity field from the balance of the remaining terms subject to the boundary conditions ($u_x = U$ at $y = H$ and $u_x = 0$ at $y = 0$) gives the steady-state flow profile,

$$u_x(y) = \frac{U \sinh(\alpha y)}{\sinh(\alpha H)}. \tag{10}$$

The resultant steady-state volume flow rate Q through a central cross section [as shown in Fig. 1(a)] with width L can be computed by integration of the flow field, $Q = \int_{y=0}^{H} u_x(y) L dy$, to obtain

$$Q = ULH\left[\frac{1}{\alpha H}\tanh\left(\frac{\alpha H}{2}\right)\right]. \tag{11}$$

In the above, note that ULH is an expected scale for a volumetric flow, while the expression in brackets is a nondimensional correction factor.

2. Numerical setup

Next we model this flow using our proposed model with static regularized Stokeslets between the plates, and compute the volume flow rate through the central cross section. Since the expression for volume flow rate [Eq. (11)] depends on the resistance α, this will establish a relation between α and $\{\rho, \varepsilon\}$ of our proposed model. In order to be able to include the regularized Stokeslets numerically, we model the flow situation using a boundary element method (BEM) [58]. In Appendix, we present results of the validation of the BEM for a Newtonian fluid between two plates.

First consider a box-shaped domain D of width and length L [see Fig. 1(a)] between the two infinitely long parallel plates. The top and bottom surfaces of this domain move with velocity $U\hat{\mathbf{x}}$ and 0, respectively. The right, left, front, and back surfaces move with the local fluid velocity. According to the BEM, the Stokes flow at $\mathbf{x_0}$ inside a bounded domain D or its boundary ∂D (faces of the box in our case) can be expressed in terms of surface forces ($\mathbf{F}$) and velocities ($\mathbf{u}$) on the boundary via boundary integral equations [58],

$$\frac{u_j(\mathbf{x}_0)}{\beta} = \frac{1}{8\pi\mu}\int_{\partial D} S_{ij}(\mathbf{x}-\mathbf{x}_0)F_i(\mathbf{x})dA - \frac{1}{8\pi}\int_{\partial D} u_i(\mathbf{x})T_{ijk}(\mathbf{x}-\mathbf{x}_0)n_k dA, \tag{12}$$

where

$$\beta = \begin{cases} 1 & \text{for } \mathbf{x}_0 \in D, \\ 2 & \text{for } \mathbf{x}_0 \in \partial D. \end{cases} \tag{13}$$

Here, μ is the fluid viscosity, $S_{ij}(\mathbf{r}) = (\delta_{ij}/|\mathbf{r}| + r_i r_j/|\mathbf{r}|^3)$ is the (singular) Stokeslet, $T_{ijk}(\mathbf{r}) = -6r_j r_j r_k/|\mathbf{r}|^5$ is the stresslet, and n_k is the unit normal of the boundary pointing into the domain. We discretized the domain boundary (∂D) into triangular elements [59] and use Gaussian quadrature rules to numerically compute the surface integrals in the above equation. When there are N_p regularized Stokeslets in the fluid domain, the fluid velocity at a point $\mathbf{x}_0$ is then calculated as

$$\begin{aligned}\frac{u_j(\mathbf{x}_0)}{\beta} = {} & \frac{1}{8\pi\mu}\sum_{b=1}^{N_b}\sum_{g=1}^{N_g} w^{(g)} S_{ij}(\mathbf{x}^{(b,g)}-\mathbf{x}_0)F_i(\mathbf{x}^{(b,g)})\Delta A^{(b)} \\ & -\frac{1}{8\pi}\sum_{b=1}^{N_b}\sum_{g=1}^{N_g} w^{(g)} u_i(\mathbf{x}^{(b,g)})T_{ijk}(\mathbf{x}^{(b,g)}-\mathbf{x}_0)n_k\Delta A^{(b)} + \sum_{p=1}^{N_p} S^{\varepsilon}_{ij}(\mathbf{x}^{(p)}-\mathbf{x}_0)f^{\varepsilon}_i(\mathbf{x}^{(p)}),\end{aligned} \tag{14}$$

where N_b is the number of boundary elements, N_g is the number of Gaussian quadrature points with weights $w^{(g)}$, the value of β depends on the position $\mathbf{x}_0$ according to Eq. (13), $\mathbf{x}^{(b,g)}$ is the gth quadrature point of the bth triangulated boundary element, $\Delta A^{(b)}$ is the area of the bth boundary element, N_p is the number of regularized Stokeslets representing the proposed porous medium model, $\mathbf{x}^{(p)}$ is the position of the pth regularized Stokeslet, and $\mathbf{f}^{\varepsilon}(\mathbf{x}^{(p)})$ is the force acting on the pth regularized Stokeslet. We used $N_b = 2480$ boundary elements and $N_g = 33$ Gaussian quadrature points generated using the algorithm in [59] and projected onto the surface as described in [60], and assumed constant force and velocity on each boundary element.

Applying Eq. (14) with $\mathbf{x}_0$ at the centers of each boundary element yields $3N_b$ equations in terms of the $3N_b$ components of boundary forces, $3N_b$ components of boundary velocities, and $3N_p$ regularized Stokeslet forces. Applying Eq. (14) at the locations of the regularized Stokeslets ($\mathbf{x}_0 = \mathbf{x}^{(p)}$) yields $3N_p$ additional equations in terms of the same variables, once the velocities at the regularized Stokeslet locations are set to zero to satisfy the static condition. Note that setting the velocity at the position of the Stokeslet to zero would not be possible if singular Stokeslets were used instead. Physically, as the regularized Stokeslets are fixed in place, the forces required to keep them stationary produces the effect of the porous medium on the flow. The solution to the above system of equations then requires $3N_b$ additional conditions, which can be obtained by specifying three of the force and velocity components $\{F_x, F_y, F_z, u_x, u_y, u_z\}$ for each boundary element, as described in what follows.

First, from the problem definition, the top plate moves to the right with velocity U and the bottom plate is stationary. Thus, at the top face of the box,

$$u_x = U, \quad u_y = 0, \quad u_z = 0, \tag{15}$$

and at the bottom face of the box,

$$u_x = 0, \quad u_y = 0, \quad u_z = 0. \tag{16}$$

Furthermore, as there is no imposed pressure gradient, we choose the value of pressure such that $F_x = 0$ on the right and left faces. Strictly speaking, the force F_x which is zero is the volume-averaged force (similar to the volume-averaged velocities and pressures in the Brinkman equation), not the microscopic force affected by the randomly placed regularized Stokeslets. Below, we also prescribe the rest of the boundary conditions in terms of volume-averaged, macroscopic quantities. This is justified *post hoc* by the independence of the results from the surface placement, i.e., the geometry of the box.

The symmetries of the problem determine enough of the remaining boundary forces and velocities to solve the problem. The box-shaped domain is an arbitrary portion of width and length L between the two infinite plates. Thus the solution in the box has translational symmetry in the x and z directions, and is also symmetric when reflected about the xy plane. Due to translational symmetry, the velocity field only depends on y, so the incompressibility condition ($\nabla \cdot \mathbf{u} = 0$) and the boundary conditions at the top and bottom plates imply that u_y is zero all along the right, left, front, and back faces. Together, reflection and translational symmetry imply that u_z is zero on the right and left faces of the box: for a u_z at some point on the right or left face, reflection about the xy plane implies that the velocity at its reflected image location is $-u_z$, but the velocity at the image location is also u_z by translation symmetry, and hence must be zero. The same argument applies to F_z on the right and left faces, and to u_z on the front and back faces. Translation symmetry in the z direction implies that the stress tensor is the same on front and back faces. Since the direction of normal changes sign for these faces, the direction of traction forces on the faces also changes sign. However, reflection symmetry about the xy plane implies that F_x and F_y are the same on the front and back faces, so they must be zero. Note that on the front and back faces, symmetry does not prohibit a nonzero F_z, which corresponds to a normal stress difference.

Collecting these together, we know that on the right and left faces, $F_x = 0$, $u_y = 0$, $u_z = 0$, and $F_z = 0$. On the front and back faces, we know that $F_x = 0$, $F_y = 0$, $u_y = 0$, and $u_z = 0$. To solve the linear system, we only need to specify six of these conditions in addition to Eqs. (15) and (16). In the following, we chose $F_x = 0$, $u_y = 0$, and $u_z = 0$ on the right and left faces, and $F_x = 0$, $F_y = 0$, and $u_z = 0$ on the front and back faces, and solve for all other variables. In the Appendix, we validate this BEM and choice of conditions for the case in which there is Newtonian fluid, not porous medium, between the plates.

The effective volume flow rate was computed by triangulating the central cross section (the plane at $x = 0$) and computing the area integral of velocity using one Gaussian quadrature point on each triangle [Eq. (14)] with $\beta = 1$, as the evaluation point is interior to the domain. The velocity field at these locations is the summation of velocity fields due to the boundary elements,

and the forces at regularized Stokeslets representing the porous medium. The net volume flow rate thus computed was compared to the analytical expression in Eq. (11) to obtain a value of the resistance α of the porous medium. A dimensional analysis reveals that the flow rate can be expressed as $Q = UL^2Q^*$. Due to linearity in U, Q^* is a dimensionless function of only the geometrical configuration of the box as well as the random distribution of regularized Stokeslets. All geometrically similar configurations (scaled by the length scale L) have the same Q^*, so it is sufficient to perform simulations with a single arbitrary value of each of U and L, and only vary the geometrical parameters $\{\rho L^3, \varepsilon/L, H/L\}$. We performed many such numerical experiments using different values of number densities (ρ), blob parameters (ε), and box heights (H) in the ranges $(64L^{-3}, 800L^{-3})$, $(2 \times 10^{-4}L, 1.5 \times 10^{-2}L)$ and $(0.1L, 0.25L)$, respectively, to obtain an estimate of α for each case. For the highest density and the porous media volume that we used, the number of Stokeslets was ∼4000.

In order for a random distribution of regularized Stokeslets to adequately represent a porous medium, we expect that the distribution must appear homogeneous on the scale of the porous medium geometry. To investigate when this holds true, we plot in Fig. 1(b) the coefficient of variation (ratio of standard deviation to the mean) obtained from the estimates of α as a function of the ratio of box height H to blob size ε, and the ratio of box height H to mean Stokeslet separation $\rho^{-1/3}$. Each data point in Fig. 1(b) is obtained from five different random distributions of regularized Stokeslets with a fixed density ρ and blob size ε. The coefficient of variation should be small if the distribution is homogeneous on the scale of the porous medium. The plot shows that the coefficient of variation is small (<0.05) as long as $H/\varepsilon > 40$ and $H\rho^{1/3} > 2$ [dashed lines in Fig. 1(b)], i.e., as long as the blob size and Stokeslet spacing is small enough compared to the smallest geometrical dimension, i.e., H in our simulations. Note that for a fixed large epsilon ($H/\varepsilon < 40$), the coefficient of variation has nonmonotonic dependence on density, becoming large in the large-ε, large-ρ regime. In this regime, upon closer investigation we found that if we manually remove all regularized Stokeslets located within ε of the boundary, the coefficient of variation becomes small. Such a procedure changes the geometry; however, this behavior indicates that the large variations in this regime arise when regularized Stokeslets are randomly placed within a blob size of the boundary elements of the domain, which can lead to spatial variations in the velocities and tractions at the box surface, contrary to our prescription of boundary conditions as macroscopic quantities.

A plot of α against ρ, nondimensionalized by the length scale ε, is shown in Fig. 1(c). In this plot, we only include data points corresponding to $H/\varepsilon > 40$, $H\rho^{1/3} > 2$, i.e., with coefficient of variation <0.05. The resistance of a porous medium, α, increases with increasing density and blob size of regularized Stokeslets. Each data point in Fig. 1(c) is obtained by averaging α values computed from five different random distributions of regularized Stokeslets with a fixed density ρ and blob size ε. The error bars correspond to the standard deviation of those five values. We confirmed that the mean value did not change appreciably, i.e., by more than the error, if more simulations were used, by computing 15 simulations for two cases. The curves obtained for different values of H/L collapse to a single curve, indicating that the box geometry H does not influence the value of α when the box dimensions are not comparable to the length scales involved in the regularized Stokeslets distribution. This is a useful result, as we can estimate the value of α (resistance in Brinkman description) from the random distribution density (ρ) and blob size (ε) of regularized Stokeslets in three dimensions (3D). It can be seen that $\alpha\varepsilon$ scales according to $(\alpha\varepsilon)^2 \sim \rho\varepsilon^3$ by the linear fit to the data (obtained while forcing a zero intercept) in Fig. 1(c).

To further validate our results, we compare the flow field as a function of height y in the box calculated from our proposed model, to the flow field obtained using the analytical solution in the Brinkman medium [Eq. (10)] with matching resistance for one case of $\{\rho, \varepsilon\}$ (Fig. 2). Note that the velocities and pressures in the Brinkman equation are the volume-averaged quantities homogenized over the spatial variation of the porous medium. In our numerical model, we also must compute a volume-averaged flow to homogenize variations near regularized Stokeslets. The volume average for our numerical model is computed over a cube of size $\rho^{-1/3}$. The flow fields of our model and

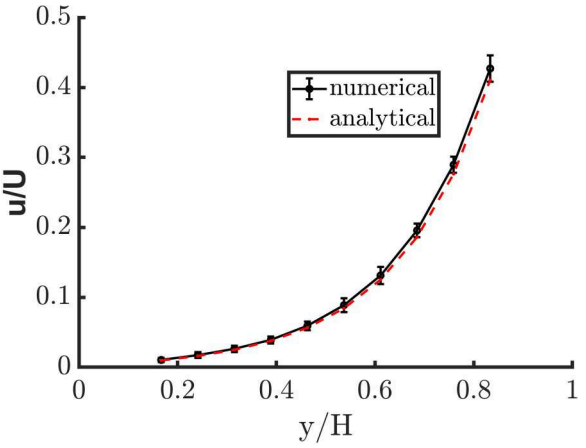

FIG. 2. Volume-averaged x component of the velocity (normalized by the top surface velocity U) as a function of height y (normalized with the box's height H) computed numerically using the proposed model, compared to the analytically computed flow field in a Brinkman medium with corresponding resistance α. The velocity field is computed at $x = 0$, the central cross section of the box. The error bars represent the standard deviation in the flow field across five different z positions, $z/L = (-1/3, -1/6, 0, 1/6, 1/3)$. The values of ρL^3, ε/L, αL, and H/L used to generate the data in this plot are 6400, 0.0025, 14.24, and 0.375, respectively.

the Brinkman medium agree well, with little variation among velocities calculated at different z coordinates but the same height in the box (displayed as error bars).

B. Source flow

We carried out a second numerical experiment to further corroborate the results obtained in Sec. III A. Consider a source at the origin forcing a spherically symmetric flow through a shell of porous medium [Fig. 3(a)]. A point source with constant volume outflow Q and viscosity μ is placed at the center of a porous shell of inner radius R and thickness t. Due to the porous medium's resistance, constant pressure is generated inside the shell after a steady flow is established.

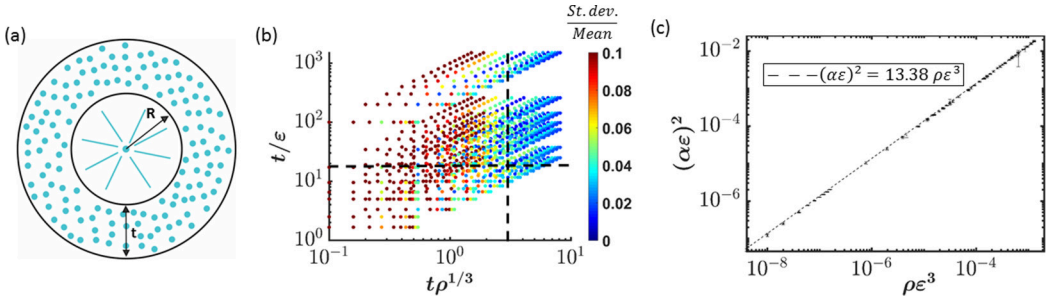

FIG. 3. (a) A point source with constant volume outflow Q is surrounded by a shell of porous medium, generating a pressure inside the shell. (b) Plot showing the ratio of standard deviation to the mean for estimates of α for a given combination of $\{\rho, \varepsilon\}$, and shell thickness t. (c) Plot showing the dependence of nondimensional Brinkman medium resistance $\alpha\varepsilon$ on the nondimensional density $\rho\varepsilon^3$ of regularized Stokeslets. The results are independent of the shell geometry.

1. Analytical solution

The resistance α of the Brinkman medium determines the pressure developed inside the shell, as shown below. We solve Eq. (1) in the spherical coordinate system, where only the radial component is nonzero,

$$-\frac{\partial p}{\partial r} = -\mu\left[\frac{1}{r^2}\frac{\partial}{\partial r}\left(r^2\frac{\partial u_r}{\partial r}\right) - \frac{2u_r}{r^2}\right] + \mu\alpha^2 u_r, \tag{17}$$

where u_r is the radial component of the velocity $\mathbf{u}$ and r is the radial distance. The solution is $u_r = Q/(4\pi r^2)$, which is the same as in a Newtonian fluid due to incompressibility. Substituting the value of u_r into Eq. (17) and integrating from R to $R+t$ gives an expression for the pressure generated across the thickness of the shell, Δp. This expression can be used to compute the value of α:

$$\alpha^2 = \frac{1}{R^2}\left[4\pi\left(1+\frac{R}{t}\right)\frac{R^3\Delta p}{\mu Q}\right]. \tag{18}$$

2. Numerical setup

Numerically, we represent the Brinkman medium by placing static regularized Stokeslets in the thickness of the spherical shell. To do so, we first randomly distributed Stokeslets at an appropriate density in the smallest cube that fits the spherical shell. Then, we removed the Stokeslets that are not in the thickness of the shell. The constant volume outflow from the point source located at the center of the shell pushes these regularized Stokeslets radially outward with local fluid velocity, and consequently an opposing force is required to keep each of these regularized Stokeslets static. The flow field $\mathbf{u}$ at $\mathbf{x}_0$ is

$$u_j(\mathbf{x}_0) = \frac{Q}{4\pi|\mathbf{x}_0|^3}x_{0j} + \sum_{p=1}^{N_p} S_{ij}^{\varepsilon}(\mathbf{x}^{(p)} - \mathbf{x}_0) f_i^{\varepsilon}(\mathbf{x}^{(p)}), \tag{19}$$

where N_p is the number of regularized Stokeslets, $\mathbf{x}_p$ is the location of the pth regularized Stokeslet, and $\mathbf{f}^{\varepsilon}(\mathbf{x}^{(p)})$ is the force acting on the pth regularized Stokeslet. Forces acting on each regularized Stokeslet can be computed by solving the system of equations obtained by applying the above equation with $\mathbf{x}_0$ at the center of each regularized Stokeslet and imposing zero velocity on them $[\mathbf{u}(\mathbf{x}^{(p)}) = 0]$. These forces develop pressure P at the center of the shell found by evaluating Eq. (8) at the origin [34],

$$P = \sum_{p=1}^{N_p} \frac{2|\mathbf{x}^{(p)}|^2 + 5\varepsilon^2}{(|\mathbf{x}^{(p)}|^2 + \varepsilon^2)^{5/2}} x_i^{(p)} f_i^{\varepsilon}(\mathbf{x}^{(p)}). \tag{20}$$

The pressure in the far field outside the spherical shell is zero. The numerical value of the pressure difference across the porous shell thus obtained was compared to the analytical expression in Eq. (18). A dimensional analysis reveals that the pressure difference can be expressed as $\Delta p = (\mu Q/R^3)\Delta p^*$. Due to linearity in μ and Q, Δp^* is a dimensionless function of only the geometrical configuration of the shell as well as the random distribution of regularized Stokeslets. All geometrically similar configurations (scaled by the length scale R) have the same Δp^*, so it is sufficient to perform simulations with a single arbitrary value of each of Q, μ, and R, and only vary the geometrical parameters $\{\varepsilon/R, \rho R^3, t/R\}$.

In Fig. 3(b), we plot the coefficient of variation (ratio of standard deviation to the mean) obtained from the estimates of α as a function of the ratio shell thickness t to blob size ε, and mean Stokeslet separation $\rho^{-1/3}$ for different values of ρ, ε, and t in the range $(0.125R^{-3}, 160R^{-3})$, $(10^{-3}R, 0.12R)$, and $(0.1R, 3R)$, respectively. For the highest density and the porous media volume that we used, the number of Stokeslets was ∼7000. Each data point is obtained from five different random distributions of regularized Stokeslets with a fixed density ρ and blob size ε. The coefficient

of variation should be small if the distribution is homogeneous on the scale of the porous medium. It can be seen that the coefficient of variation is small (<0.05) as long as $t/\varepsilon > 20$ and $t\rho^{1/3} > 3$ [dashed lines in Fig. 3(b)]. Again, this shows that a random distribution of regularized Stokeslets can adequately describe the shell geometry as long as the blob size and Stokeslet spacing is small enough compared to a typical length scale of the geometry; otherwise, the distribution of Stokeslets is not sufficiently uniform to represent a Brinkman medium.

Using ε as the length scale, α and ρ are nondimensionalized and plotted in Fig. 3(c). In this plot, we only include data points corresponding to $t/\varepsilon > 20$, and $t\rho^{1/3} > 3$, i.e., with coefficient of variation <0.05. Each data point is obtained by averaging α values computed from five different random distributions of regularized Stokeslets with a fixed density ρ and blob size ε. The error bars correspond to the standard deviation of those five values. As for the Couette flow, all the results from different geometries collapse onto a single curve, showing that the thickness t and radius R do not influence the nondimensional α. In other words, the experimental geometry does not influence the value of α, and we get an estimate of the resistance of porous medium from only the density and blob size of the regularized Stokeslets arrangement. It can be seen from Fig. 3(c) that $\alpha\varepsilon$ scales according to $(\alpha\varepsilon)^2 \sim \rho\varepsilon$ by the linear fit to the data (forcing a zero intercept).

IV. EXAMPLES

In this section, we demonstrate our proposed method using two examples of microswimmers swimming in heterogeneous environments. The first explores how swimming is affected by the approach towards a particle made of porous media. The second examines how swimming is affected by confinement by the porous media.

A. Squirmer approaching a porous sphere

Microorganisms must approach other organisms and particles in order to feed, mate, and find new habitats [61]. However, in the low-Reynolds number microscale environment, such approach is constrained by viscous interactions. These viscous interactions have been studied previously for the approach to solid particles [61]. However, some objects that may be approached by microorganisms are porous. In particular, sinking organic matter in the ocean,"marine snow," is porous [62] and attracts organisms which seek to use it as a nutrient source. Here, we investigate a simple model investigating how the porous, instead of solid, nature of marine snow affects the ability of microorganisms to approach it.

We calculate the swimming speed V of a spherical squirmer swimmer of radius $a = 1\ \mu$m approaching a stationary sphere of radius $2a$ composed of porous media. The squirmer and sphere surfaces are separated by a distance d [Fig. 4(a)]. The squirmer swims due to the prescribed slip velocities at its surface [63] and is a common model for the swimming of ciliated microorganisms such as paramecia or *Volvox* algae. In our case, the slip velocities on the squirmer surface (relative to the squirmer itself) are specified by

$$\mathbf{V}_s = \left(B_1 \sin\theta + \frac{B_2}{2}\sin 2\theta\right)\hat{\boldsymbol{\theta}} \tag{21}$$

in spherical coordinates $\{r, \theta, \phi\}$ defined from the center of the squirmer sphere, where θ is the angle from the direction towards the stationary sphere, which is also the direction of the swimming velocity. The basis vector $\hat{\boldsymbol{\theta}}$ points in the direction of increasing θ. We use $B_2/B_1 = -1$. To find the swimming velocity of the squirmer, we fill the stationary sphere with a random distribution of regularized Stokeslets, with a blob size and density that produce various values of resistance α, as described in the previous sections. We test seven different resistances: $\alpha = 0.5255\ \mu\text{m}^{-1}$ ($\rho = 20\ \mu\text{m}^{-3}$, $\varepsilon = 1 \times 10^{-3}\ \mu$m), $\alpha = 1.4393\ \mu\text{m}^{-1}$ ($\rho = 30\ \mu\text{m}^{-3}$, $\varepsilon = 5 \times 10^{-3}\ \mu$m), $\alpha = 2.7560\ \mu\text{m}^{-1}$ ($\rho = 55\ \mu\text{m}^{-3}$, $\varepsilon = 1 \times 10^{-2}\ \mu$m), $\alpha = 4.0709\ \mu\text{m}^{-1}$ ($\rho = 60\ \mu\text{m}^{-3}$, $\varepsilon = 2 \times 10^{-2}\ \mu$m), $\alpha = 5.7571\ \mu\text{m}^{-1}$ ($\rho = 120\ \mu\text{m}^{-3}$, $\varepsilon = 2 \times 10^{-2}\ \mu$m), $\alpha =$

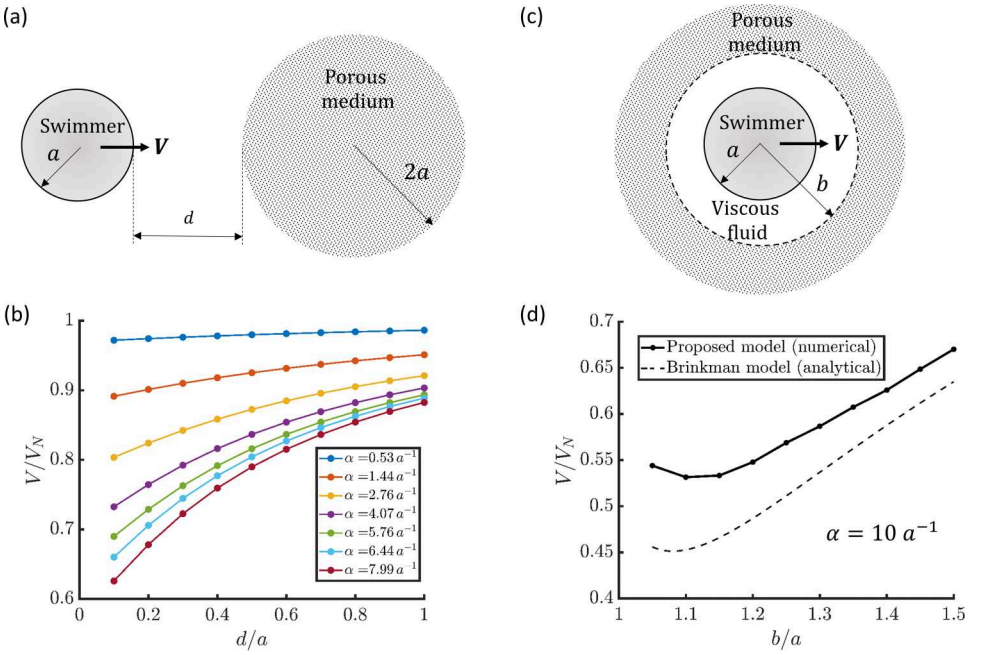

FIG. 4. (a) Schematic of spherical squirmer approaching a stationary spherical particle made of porous medium. (b) Swimming velocity (V) of squirmer approaching a porous stationary particle as a function of separation distance d. Velocity is normalized by swimming velocity in the absence of the particle (V_N). (c) Schematic of spherical squirmer confined in a spherical pocket of fluid bounded by porous medium. (d) Swimming velocity of squirmer confined as in (c) as a function of confinement size.

6.4366 μm^{-1} ($\rho = 150\ \mu\text{m}^{-3}$, $\varepsilon = 2 \times 10^{-2}\,\mu\text{m}$), $\alpha = 7.9876\ \mu\text{m}^{-1}$ ($\rho = 230\ \mu\text{m}^{-3}$, $\varepsilon = 2 \times 10^{-2}\ \mu\text{m}$).

The velocity at the locations of the regularized Stokeslets in the stationary sphere is specified to be zero. We discretize the surface of the squirmer with 6146 regularized Stokeslets with $\varepsilon = 2.08 \times 10^{-2}\ \mu\text{m}$, which is approximately equal to one-third of the spacing between them [36], and we specify the velocity at the locations $\mathbf{r}^q$ of each of these regularized Stokeslets to be

$$\mathbf{v}(\mathbf{r}^q) = \mathbf{V}_s(\mathbf{r}^q) + \mathbf{V} + \boldsymbol{\Omega} \times \mathbf{r}^q. \tag{22}$$

In this equation, $\mathbf{V}$ is the translational velocity of the squirmer and $\boldsymbol{\Omega}$ is the angular velocity of the squirmer relative to its center. The location $\mathbf{r}^q$ is also measured relative to the center of the squirmer. The values of $\mathbf{V}$ and $\boldsymbol{\Omega}$ are determined by finding regularized Stokeslet forces such that the velocity field satisfies the velocities specified at the locations of the regularized Stokeslets, plus force- and torque-free conditions on the squirmer [37].

In the absence of the stationary sphere, the swimming velocity of a free squirmer is $V_N = 2B_1/3$ [61]. Figure 4(b) shows the swimming speed V calculated in the presence of the stationary sphere with different resistances α. The plotted results do not depend on the value of B_1 since the swimming speed is normalized by the free squirmer velocity. Since $V/V_N < 1$, the presence of the sphere reduces the swimming speed. However, a porous obstacle does not reduce the swimming speed as much as a solid one; as the resistance increases, the reduction also increases. Thus we expect the approach of microorganisms to porous particles such as marine snow to be less hindered by viscous effects than the corresponding approach to solid particles.

B. Squirmer within spherical pocket bounded by porous medium

As mentioned in Sec. I, *Helicobacter pylori* swims in a fluid pocket while traversing the gastric mucus that it generates by producing ammonia, which neutralizes its surroundings and thereby locally fluidizes nearby mucus [22]. The effect of this type of three-dimensional confinement in a pocket has been studied by examining spherical squirmer swimmers inside spherical domains of fluid with either a more viscous fluid [64] or Brinkman fluid [65] outside the interior domain. Here, we use our proposed method to solve the problem of a spherical squirmer of radius $a = 1\ \mu$m at the center of a spherical pocket of radius b [Fig. 4(c)], surrounded by a porous medium with resistance $\alpha = 10\,a^{-1}$.

We model the porous medium using a random distribution of regularized Stokeslets with blob size $\varepsilon = 0.01\ \mu$m and density $\rho = 725\ \mu\text{m}^{-3}$ to correspond with $\alpha = 10\ \mu\text{m}^{-1}$. The porous medium is only modeled for a spherical shell of thickness $0.9\ \mu$m. Note that this thickness corresponds to nine Brinkman decay lengths, so the velocity field is expected to nearly entirely diminish within the shell. The squirmer swims due to prescribed tangential velocity as described above [Eq. (21)] and is also modeled using regularized Stokeslets in the same way as described above. The swimming velocity of the squirmer as a function of confining sphere size b is shown in Fig. 4(d). An analytic solution for this geometry and resistance is available from Nganguia *et al.* [65] and is shown for comparison. Nganguia *et al.* emphasize that the confinement slows down the squirmer, but in a nonmonotonic fashion as the pocket size increases.

Like the analytic solution, we find that the squirmer is slowed by confinement in a nonmonotonic fashion with a minimum around $b = 1.1a$. However, the two models do not match quantitatively. A key difference between our approach and the analytic solution is that the analytic model specifies boundary conditions for the macroscopic averaged fields (continuous velocity and traction) at the interface between the fluid and Brinkman medium, but our proposed model only involves (continuous) microscopic flow fields.

The boundary conditions for interfaces of Brinkman media with Newtonian fluid [16,66–70] or between two different Brinkman media [15] are a matter of current study. This example highlights the importance of the boundary conditions for macroscopic continuum descriptions of porous media such as the Brinkman model. Our proposed model, on the other hand, does not have any freedom in choosing boundary conditions and may be considered a microscale model of porous medium in its own right. Indeed, models that, like ours, represent porous media using discrete elements [71–73] have been used to investigate both the validity of the Brinkman model as well as its associated boundary conditions. Studying the effects of heterogeneous media using our model in comparison with the Brinkman model can be used to clarify which effects are not dependent on the choice of boundary conditions, such as the nonmonotonic slowing down of tangential squirmers in spherical confinement.

V. DISCUSSION AND CONCLUSIONS

We have found that the square of Brinkman medium resistance α has a linear relation with the density ρ and blob size ε of regularized Stokeslets that represent the same porous medium. The results from the Couette flow and source flow experiments can be written as $\alpha = 3.72\sqrt{\rho\varepsilon}$ and $\alpha = 3.66\sqrt{\rho\varepsilon}$, respectively. The difference in proportionality constants of these relations corresponds to $\sim$2% error in the estimates of α for a given ρ and ε. The agreement between the two experiments can also be established by directly comparing the mean resistance estimates obtained from the two experiments at the same ρ and ε. We plot the ratio of estimates from the two numerical experiments against the parameter $\rho\varepsilon^3$ for each input pair $\{\rho, \varepsilon\}$ in Fig. 5. In this plot, we only include the subset of data points from Figs. 1(c) and 3(c) which have common values of ρ and ε. The ratios in Fig. 5 are clustered around 1, mostly within 4% error. This low difference in values of α from two independent numerical experiments corroborates the overall relation of α to $\sqrt{\rho\varepsilon}$.

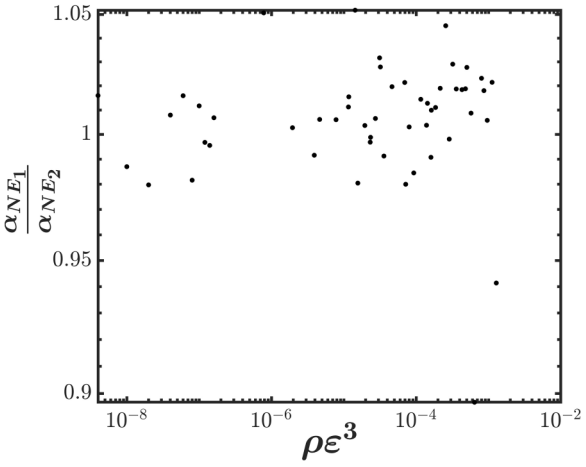

FIG. 5. Plot showing the ratio of the resistance estimate α_{NE_1} from the first numerical experiment to the resistance estimate α_{NE_2} from the second numerical experiment, for each pair of density ρ and blob size ε, plotted as a function of $\rho\varepsilon^3$.

There are multiple ways to estimate the volume fraction of the porous medium described by our random collection of regularized Stokeslets which yield results of the same order of magnitude. First, one can estimate the volume of regularized Stokeslets by considering each regularized Stokeslet to have the volume of a sphere with radius given by the blob size ($4\pi\varepsilon^3/3$). Then the volume fraction of fluid is ($1 - 4\pi\rho\varepsilon^3/3$). Second, the volume can be estimated from the results of Spielman and Goren [74], who derived a formula for the volume fraction (ϕ) of the fluid in terms of α for a random collection of *fibers* of radius ε (different from the pointlike regularized Stokeslets we use) as

$$\phi = \frac{\alpha\varepsilon K_0(\alpha\varepsilon) + 10K_1(\alpha\varepsilon)}{4\alpha\varepsilon K_0(\alpha\varepsilon) + 10K_1(\alpha\varepsilon)}, \tag{23}$$

where $K_0(.)$ and $K_1(.)$ are the zeroth- and first-order modified Bessel functions of the second kind. The same formula has been used [27] to compute the volume fractions of biological fluids from values of α. The result of applying this equation to the numerical experiments is shown in Fig. 6. From Fig. 6, it can be seen that the solid volume fraction of the first estimate ($4\pi\rho\varepsilon^3/3$) is of the same order of magnitude as that from the second estimate ($1 - \phi$). The error bars in the volume fraction plot are propagated from the error in the estimates of α from Secs. III A and III B. Overall, it can be seen that the volume fraction of solid is quite low, so that the Brinkman model is expected to apply. However, the errors increase as the density increases, perhaps because the Brinkman description of a porous medium becomes less valid as one leaves the dilute limit.

In this paper, we have shown that the flows inside a porous medium which obey Brinkman equations can be described numerically by placing many static regularized Stokeslets randomly in three dimensions. Using numerical experiments, we have shown that we can estimate the resistance α of a corresponding Brinkman medium. The α of an equivalent Brinkman medium can be used to compute the permeability κ ($= \alpha^{-2}$) and the porosity ϕ [using Eq. (23)]. Thus one can fully characterize the Brinkman medium from the values of ρ and ε of a regularized Stokeslet arrangement.

The main limitation on our method is that the length scales of the regularized Stokeslets distribution, $\{\rho^{-1/3}, \varepsilon\}$, should be small compared to the typical length scales of the domain of porous media. For example, we found that sufficient homogeneity is provided when the blob size was less than a 40th (20th) and the mean separation distance between the Stokeslets was less than one-half

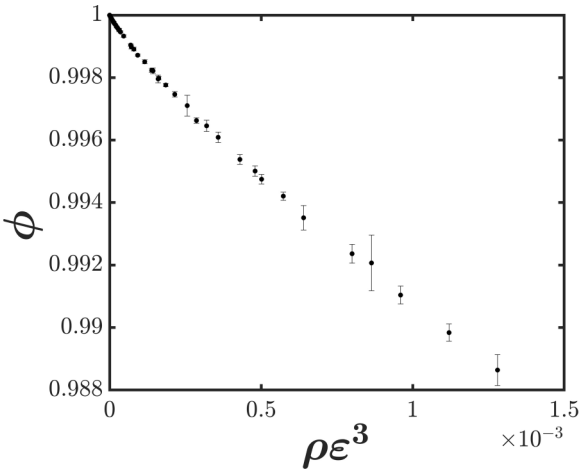

FIG. 6. Volume fraction ϕ of fluid inside a Brinkman medium, estimated from Eq. (23) for a given regularized Stokeslet arrangement of density ρ and blob size ε.

(one-third) of the height of the box (shell thickness) in our first (second) numerical experiment. If there are other boundary elements or regularized Stokeslets describing domain geometries in the computation, one must also avoid situations where the regularized Stokeslets describing the porous media are likely to approach them closely, which occurs when the blob size and density are both large. We observed such issues in the Couette flow but not in the source flow, which did not have any boundary elements describing its geometry. Such issues may be able to be ameliorated by using regularized Stokeslets with tailored blob functions such as those with compact support [75,76], or by using images [77,78] to reduce the influence of nearby plane boundaries. We also note that one of our examples highlights the fact that solutions to the Brinkman model may depend on choices for boundary conditions at the interface between the porous media and fluid.

Our model is applicable wherever a Brinkman medium is involved and is easy to implement as it just requires one to fill the volume occupied by the Brinkman medium with a random arrangement of static regularized Stokeslets of appropriate number density and blob size creating the desired resistance value α. For instance, self-propelled swimming in a homogeneous Brinkman medium has been modeled using regularized Brinkmanlets for general [27] and standard geometries [65]; we can simulate this swimming using the method of regularized Stokeslets for the swimmer geometry [35] and place regularized Stokeslets at appropriate $\{\rho, \varepsilon\}$ around the swimmer to account for the effect of the porous medium. For swimming bacteria or sperm, the flagellum would set the length scale determining the needed density of regularized Stokeslets. In order to resolve the geometry of a porous medium between the crests of a swimmer's flagellum, the density requirement could require many regularized Stokeslets; however, we note that there are many cases where, for flagellar swimming in mucus (treated as porous media), the pore sizes of the medium are actually significantly larger than the length scales of flagella. In that case, it may be more realistic for the flagellum not to directly interact with the media [17], suggesting that less dense (hence fewer) regularized Stokeslets could be used. Another possible application that our method is well suited for is to model porous media with spatially varying resistance. In that case, the density requirement for regularized Stokeslets may also need to account for the length scale over which the resistance varies. Although the implementation of our method is simple if one is already using regularized Stokeslets, due to the large number of regularized Stokeslets it can quickly become computationally costly, which might require the implementation of efficient solvers such as multipole methods [79,80]. Thus, for homogeneous domains of porous media, the method of regularized Brinkmanlets may be more appropriate, but the real advantage of our model can be seen when there is a heterogeneous medium around a moving

boundary. For example, the actively self-generated confinement of bacteria swimming through gels has only been tackled analytically using extremely simplified approaches [22,23,64] and cannot be treated with the method of regularized Brinkmanlets. In our second example, we used our method to numerically treat this problem by filling the volume of the porous gel with static regularized Stokeslets, without having to account for the complicated boundary conditions near the medium interface arising due to the change in constitutive laws. This type of approach is also similar in spirit to the treatment of viscoelastic fluids by a lattice arrangement of regularized Stokeslets interconnected by spring and dashpot elements [57].

ACKNOWLEDGMENTS

S.K.K., M.J., and H.C.F are supported by NIH Grant No. 1R01GM131408-01. H.C.F. is supported by NSF Grant No. CBET-1805847. We also acknowledge the use of computing resources from the Center for High Performance Computing at the University of Utah.

The authors declare that they have no conflict of interest.

APPENDIX: BOUNDARY CONDITIONS TO MODEL NEWTONIAN SHEAR FLOW INSIDE A BOX

When there is no porous medium between the two infinitely long plates, the fluid flow there is governed by the Stokes equation. The velocity of the top plate sliding towards the right at velocity U drives the fluid between the plates in a simple shear flow, $\mathbf{u}_{\text{Newtonian}} = Uy\hat{\mathbf{x}}/H$. As in Sec. III A 2, we model the fluid flow in a box of width and length L via BEM where the top and bottom plate move with the prescribed velocity ($U\hat{\mathbf{x}}$ and 0, respectively).

Similar to the main text, we discretize the boundary of the box into triangular elements and apply Eq. (14) with $\mathbf{x}_0$ as the centers of each triangle, but with all regularized Stokeslet forces set to zero since there is no porous medium between the plates. Then, we have a system of $3N_b$ equations, in terms of $6N_b$ components of traction force and velocity on each of the triangular elements. Thus, for each side of the box, we can only specify three of $\{F_x, F_y, F_z, u_x, u_y, u_z\}$ and the other three are obtained from solving the system of equations. All of these quantities can be calculated from the analytical solution, so below we test a large set of choices, of which quantities are specified, and examine the result of the choice on the accuracy of the BEM for the flow field within the box.

On the top and bottom face of the box, u_x comes from the problem definition and, motivated by the porous media problem, we consider F_x to be an unknown output that must be calculated. Then there are six ways to pick the remaining two input quantities from u_y, u_z, F_y, and F_z. On the right and left faces of the box, we consider u_x to be an unknown nonzero velocity field that must be calculated and, since F_y is nonzero, we do not prescribe its value. Then there are four ways to pick the three input quantities from u_y, u_z, F_x, and F_z. On the front and back faces, we also consider u_x to be an unknown velocity field to be calculated. Then there are 10 ways to pick the three input quantities from u_y, u_z, F_x, F_y, and F_z. In total, we check 240 ($6 \times 4 \times 10$) ways to prescribe the boundary conditions on the box in the BEM. The resulting system of equations can be arranged in the matrix form $AX = b$. Here, A is the coefficient matrix whose elements are the coefficients of unknown quantities in the BEM [Eq. (14)], X is the column matrix with unknown quantities, and b is the column matrix computed by substituting the input quantities in the BEM [Eq. (14)]. Then the unknown quantities are computed by solving the system of equations $AX = b$, and so we know the force and velocity of each triangular element representing the sides of the box. From these, we can compute the velocity field at different locations on the central cross section of the box using Eq. (14) with $\beta = 1$.

Comparing the numerical solution to the analytical solution $\mathbf{u}_{\text{Newtonian}}$, we compute the norm error of the velocity field on the central cross section as $\sum_{n=1}^{N_e}[|\mathbf{u}_{\text{Newtonian}} - \mathbf{u}(\mathbf{x}_n)|A_n]^2$ and normalize with $(UL)^2$, where N_e is the number of evaluation points, $\mathbf{x}_n$ is the location of the nth evaluation point on the central cross section, $\mathbf{u}$ is computed from Eq. (14), A_n is the area of the nth element, and $|\mathbf{v}|$

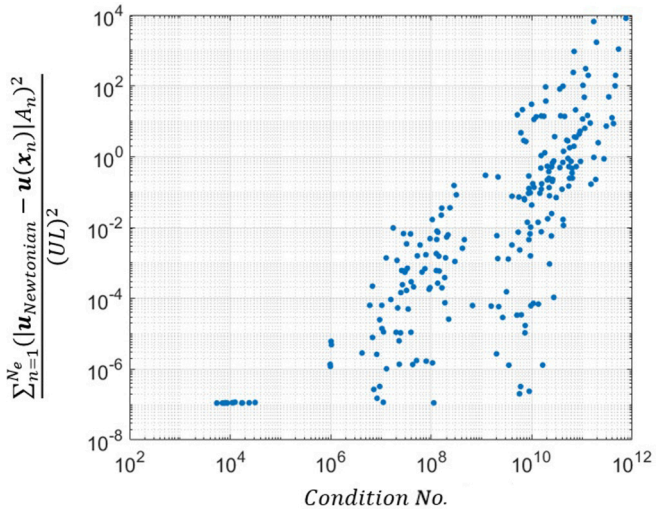

FIG. 7. Normalized error between the analytical velocity field and that computed from the boundary element formulation, for Newtonian Couette flow, plotted as a function of the condition number of coefficient matrix A (see text) for different choices of boundary conditions on the box surface. We chose U and L as velocity and length scales, respectively, to normalize the error.

is the magnitude of vector **v**. For each of 240 possible ways to set up the boundary conditions, we computed the condition number of the corresponding coefficient matrix A and the resulting norm error and plot it in Fig. 7. The region on the bottom left of the plot from condition number 5.4×10^3 to 3.1×10^4 corresponds to low condition numbers and minimum error in the velocity field. It can be seen that the boundary condition choices leading to low condition numbers give a low error in the velocity field. These accurate, low-condition-number choices correspond to cases when for each side and each direction, either the velocity or force, but not both, are specified. For example, on the right and left sides, either u_z or F_z should be specified, in addition to F_x (u_x was considered to be an unknown) and u_y (since F_y was nonzero so we considered it to be an unknown). We do not know what determines which boundary conditions are more or less well conditioned, but note that the choice of conditions used for the porous media in the main text is one of these accurate and low-condition-number choices.

[1] L. Xue, X. Guo, and H. Chen, *Fluid Flow in Porous Media: Fundamentals and Applications* (World Scientific, Singapore, 2020).

[2] K. Vafai, *Porous Media: Applications in Biological Systems and Biotechnology - 1*, 1st ed. (CRC Press, Boca Raton, FL, 2010).

[3] J. R. Philip, Flow in porous media, Annu. Rev. Fluid Mech. **2**, 177 (1970).

[4] F. J. Carrillo and I. C. Bourg, A darcy-brinkman-biot approach to modeling the hydrology and mechanics of porous media containing macropores and deformable microporous regions, Water Resour. Res. **55**, 8096 (2019).

[5] A. Riaz, M. Hesse, H. A. Tchelepi, and F. M. Orr, Onset of convection in a gravitationally unstable diffusive boundary layer in porous media, J. Fluid Mech. **548**, 87 (2006).

[6] H. A. Sheldon, A. C. Barnicoat, and A. Ord, Numerical modelling of faulting and fluid flow in porous rocks: An approach based on critical state soil mechanics, J. Struct. Geol. **28**, 1468 (2006).

[7] H. Darcy, *Les Fontaines Publiques de la Ville de Dijon: Exposition et Application* (Dalmont, Paris, 1856).

[8] G. Neale and W. Nader, Practical significance of Brinkman's extension of Darcy's law: Coupled parallel flows within a channel and a bounding porous medium, Can. J. Chem. Eng. **52**, 475 (1974).
[9] H. C. Brinkman, A calculation of the viscous force exerted by a flowing fluid on a dense swarm of particles, Appl. Sci. Res. **1**, 27 (1949).
[10] I. D. Howells, Drag due to the motion of a Newtonian fluid through a sparse random array of small fixed rigid objects, J. Fluid Mech. **64**, 449 (1974).
[11] J. Rubinstein, Effective equations for flow in random porous media with a large number of scales, J. Fluid Mech. **170**, 379 (1986).
[12] L. Durlofsky and J. F. Brady, Analysis of the Brinkman equation as a model for flow in porous media, Phys. Fluids **30**, 3329 (1987).
[13] S. Liu and J. Masliyah, Dispersion in Porous Media, in *Handbook of Porous Media* (CRC Press, Boca Raton, FL, 2005), pp. 99–160.
[14] J.-L. Auriault, On the domain of validity of Brinkman's equation, Transp. Porous Media **79**, 215 (2009).
[15] E. Ahmadi, R. Cortez, and H. Fujioka, Boundary integral formulation for flows containing an interface between two porous media, J. Fluid Mech. **816**, 71 (2017).
[16] M. Chandesris and D. Jamet, Boundary conditions at a planar fluid-porous interface for a Poiseuille flow, Intl. J. Heat Mass Transf. **49**, 2137 (2006).
[17] H. C. Fu, V. B. Shenoy, and T. R. Powers, Low-Reynolds-number swimming in gels, Europhys. Lett. **91**, 24002 (2010).
[18] I. D. Howells, Drag on fixed beds of fibres in slow flow, J. Fluid Mech. **355**, 163 (1998).
[19] K. G. Link, M. G. Sorrells, N. A. Danes, K. B. Neeves, K. Leiderman, and A. L. Fogelson, A mathematical model of platelet aggregation in an extravascular injury under flow, Multiscale Model. Simul. **18**, 1489 (2020).
[20] W. E. Uspal and P. S. Doyle, Self-organizing microfluidic crystals, Soft Matter **10**, 5177 (2014).
[21] K. M. Arthurs, L. C. Moore, C. S. Peskin, E. B. Pitman, and H. E. Layton, Modeling arteriolar flow and mass transport using the immersed boundary method, J. Comput. Phys. **147**, 402 (1998).
[22] S. A. Mirbagheri and H. C. Fu, *Helicobacter pylori* Couples Motility and Diffusion to Actively Create a Heterogeneous Complex Medium in Gastric Mucus, Phys. Rev. Lett. **116**, 198101 (2016).
[23] H. Nganguia, L. Zhu, D. Palaniappan, and O. S. Pak, Squirming in a viscous fluid enclosed by a Brinkman medium, Phys. Rev. E **101**, 063105 (2020).
[24] J. Feng, P. Ganatos, and S. Weinbaum, Motion of a sphere near planar confining boundaries in a Brinkman medium, J. Fluid Mech. **375**, 265 (1998).
[25] U. S. Mahabaleshwar, P. N. Vinay Kumar, K. R. Nagaraju, G. Bognár, and S. N. Ravichandra Nayakar, A new exact solution for the flow of a fluid through porous media for a variety of boundary conditions, Fluids **4**, 125 (2019).
[26] A. N. Filippov, D. Y. Khanukaeva, S. I. Vasin, V. D. Sobolev, and V. M. Starov, Liquid flow inside a cylindrical capillary with walls covered with a porous layer (Gel), Colloid J. **75**, 214 (2013).
[27] N. Ho, K. Leiderman, and S. Olson, A three-dimensional model of flagellar swimming in a Brinkman fluid, J. Fluid Mech. **864**, 1088 (2019).
[28] K. Leiderman and S. D. Olson, Swimming in a two-dimensional Brinkman fluid: Computational modeling and regularized solutions, Phys. Fluids **28**, 021902 (2016).
[29] M. Kohr, G. P. R. Sekhar, and J. R. Blake, Green's function of the Brinkman equation in a 2D anisotropic case, IMA J. Appl. Math. **73**, 374 (2007).
[30] T. Levy, Fluid flow through an array of fixed particles, Intl. J. Eng. Sci. **21**, 11 (1983).
[31] R. Dillon and L. Fauci, A microscale model of bacterial and biofilm dynamics in porous media, Biotechnol. Bioeng. **68**, 536 (2000).
[32] A. M. Leshansky, Enhanced low-Reynolds-number propulsion in heterogeneous viscous environments, Phys. Rev. E **80**, 051911 (2009).
[33] Y. Matsumura, D. Jenne, and T. L. Jackson, Numerical simulation of fluid flow through random packs of ellipses, Phys. Fluids **27**, 023301 (2015).
[34] R. Cortez, The method of regularized Stokeslets, SIAM J. Sci. Comput. **23**, 1204 (2001).

[35] R. Cortez, L. Fauci, and A. Medovikov, The method of regularized Stokeslets in three dimensions: Analysis, validation, and application to helical swimming, Phys. Fluids **17**, 031504 (2005).
[36] Y. Hyon, Marcos, T. R. Powers, R. Stocker, and H. C. Fu, The wiggling trajectories of bacteria, J. Fluid Mech. **705**, 58 (2012).
[37] J. D. Martindale, M. Jabbarzadeh, and H. C. Fu, Choice of computational method for swimming and pumping with nonslender helical filaments at low Reynolds number, Phys. Fluids **28**, 021901 (2016).
[38] D. J. Smith, A boundary element regularized Stokeslet method applied to cilia-and flagella-driven flow, Proc. R. Soc. A **465**, 3605 (2009).
[39] M. A. Constantino, M. Jabbarzadeh, H. C. Fu, and R. Bansil, Helical and rod-shaped bacteria swim in helical trajectories with little additional propulsion from helical shape, Sci. Adv. **2**, e1601661 (2016).
[40] M. A. Constantino, M. Jabbarzadeh, H. C. Fu, Z. Xhen, J. G. Fox, F. Haesebrouck, S. K. Linden, and R. Bansil, Bipolar lophotrichous *Helicobacter suis* combine extended and wrapped flagella bundles to exhibit multiple modes of motility, Sci. Rep. **8**, 14415(2018).
[41] K. Ishimoto, H. Gadelha, E. A. Gaffney, D. J. Smith, and J. Kirkman-Brown, Coarse-Graining the Fluid Flow around a Human Sperm, Phys. Rev. Lett. **118**, 124501 (2017).
[42] S. D. Olson, S. Lim, and R. Cortez, Modeling the dynamics of an elastic rod with intrinsic curvature and twist using a regularized Stokes formulation, J. Comput. Phys. **238**, 169 (2013).
[43] J. G. Gibbs, S. Kothari, D. Saintillan, and Y. P. Zhao, Geometrically designing the kinematic behavior of catalytic nanomotors, Nano Lett. **11**, 2543 (2011).
[44] U. K. Cheang, F. Meshkati, D. Kim, M. J. Kim, and H. C. Fu, Minimal geometric requirements for micropropulsion via magnetic rotation, Phys. Rev. E: Stat., Nonlinear, Soft Matter Phys. **90**, 033007 (2014).
[45] F. Meshkati and H. C. Fu, Modeling rigid magnetically rotated microswimmers: Rotation axes, bistability, and controllability, Phys. Rev. E **90**, 063006 (2014).
[46] H. C. Fu, M. Jabbarzadeh, and F. Meshkati, Magnetization directions and geometries of helical microswimmers for linear velocity-frequency response, Phys. Rev. E **91**, 043011 (2015).
[47] J. Ali, U. K. Cheang, J. D. Martindale, M. Jabbarzadeh, H. C. Fu, and M. J. Kim, Bacteria-inspired nanorobots with flagellar polymorphic transformations and bundling, Sci. Rep. **7**, 14098 (2017).
[48] U. K. Cheang, F. Meshkati, H. Kim, K. Lee, H. C. Fu, and M. J. Kim, Versatile microrobotics using simple modular subunits, Sci. Rep. **6**, 30472 (2016).
[49] K. Samsami, S. A. Mirbagheri, F. Meshkati, and H. C. Fu, Stability of soft magnetic helical microrobots, Fluids **5**, 19 (2020).
[50] K. Samsami, S. A. Mirbagheri, F. Meshkati, and H. C. Fu, Saturation and coercivity limit the velocity of rotating active magnetic microparticles, Phys. Rev. Fluids **5**, 064202 (2020).
[51] K. A. Rejniak, V. Estrella, T. Chen, A. S. Cohen, M. C. Lloyd, and D. L. Morse, The role of tumor tissue architecture in treatment penetration and efficacy: An integrative study, Front. Oncol. **3**, 111 (2013).
[52] Y. Aboelkassem and A. E. Staples, A bioinspired pumping model for flow in a microtube with rhythmic wall contractions, J. Fluids Struct. **42**, 187 (2013).
[53] Y. Aboelkassem and A. E. Staples, A three-dimensional model for flow pumping in a microchannel inspired by insect respiration, Acta Mech. **225**, 493 (2014).
[54] J. D. Martindale and H. C. Fu, Autonomously responsive pumping by a bacterial flagellar forest: A mean-field approach, Phys. Rev. E **96**, 033107 (2017).
[55] T. D. Montenegro-Johnson, S. Michelin, and E. Lauga, A regularised singularity approach to phoretic problems, Eur. Phys. J. E **38**, 139 (2015).
[56] B. Fogelson and A. Mogilner, Computational estimates of membrane flow and tension gradient in motile cells, PLoS One **9**, e84524 (2014).
[57] J. K. Wróbel, R. Cortez, and L. Fauci, Modeling viscoelastic networks in Stokes flow, Phys. Fluids **26**, 113102 (2014).
[58] C. C. Pozrikidis, *Boundary Integral and Singularity Methods for Linearized Viscous Flow* (Cambridge University Press, Cambridge, 1992).
[59] P.-O. Persson and G. Strang, A simple mesh generator in MATLAB, SIAM Rev. **46**, 329 (2004).

[60] C. Pozrikidis, *A Practical Guide to Boundary Element Methods with the Software Library BEMLIB* (Chapman and Hall CRC, Boca Raton, FL, 2002).
[61] M. Jabbarzadeh and H. C. Fu, Viscous constraints on microorganism approach and interaction, J. Fluid Mech. **851**, 715 (2018).
[62] A. L. Alldredge and M. W. Silver, Characteristics, dynamics and significance of marine snow, Prog. Oceanogr. **20**, 41 (1988).
[63] J. R. Blake, A spherical envelope approach to ciliary propulsion, J. Fluid Mech. **46**, 199 (1971).
[64] S. Y. Reigh and E. Lauga, Two-fluid model for locomotion under self-confinement, Phys. Rev. Fluids **2**, 093101 (2017).
[65] H. Nganguia and O. S. Pak, Squirming motion in a Brinkman medium, J. Fluid Mech. **855**, 554 (2018).
[66] F. J. Valdés-Parada, C. G. Aguilar-Madera, J. A. Ochoa-Tapia, and B. Goyeau, Velocity and stress jump conditions between a porous medium and a fluid, Adv. Water Resour. **62**, 327 (2013).
[67] S. Tlupova and R. Cortez, Boundary integral solutions of coupled Stokes and Darcy flows, J. Comput. Phys. **228**, 158 (2009).
[68] F. J. Valdes-Parada, J. Alberto Ochoa-Tapia, and J. Alvarez-Ramirez, On the effective viscosity for the Darcy-Brinkman equation, Physica A **385**, 69 (2007).
[69] F. J. Valdés-Parada, B. Goyeau, and J. A. Ochoa-Tapia, Jump momentum boundary condition at a fluid-porous dividing surface: Derivation of the closure problem, Chem. Eng. Sci. **62**, 4025 (2007).
[70] B. Goyeau, D. Lhuillier, D. Gobin, and M. Velarde, Momentum transport at a fluid-porous interface, Intl. J. Heat Mass Transf. **46**, 4071 (2003).
[71] R. E. Larson and J. J. L. Higdon, Microscopic flow near the surface of two-dimensional porous media. Part 1. Axial flow, J. Fluid Mech. **166**, 449 (1986).
[72] R. E. Larson and J. J. L. Higdon, Microscopic flow near the surface of two-dimensional porous media. Part 2. Transverse flow, J. Fluid Mech. **178**, 119 (1987).
[73] M. Sahraoui and M. Kaviany, Slip and no-slip velocity boundary conditions at interface of porous, plain media, Intl. J. Heat Mass Transf. **35**, 927 (1992).
[74] L. Spielman and S. L. Goren, Model for predicting pressure drop and filtration efficiency in fibrous media, Environ. Sci. Technol. **2**, 279 (1968).
[75] H.-N. Nguyen and R. Cortez, Reduction of the regularization error of the method of regularized Stokeslets for a rigid object immersed in a three-dimensional stokes flow, Commun. Comput. Phys. **15**, 126 (2014).
[76] B. Zhao, E. Lauga, and L. Koens, Method of regularized Stokeslets: Flow analysis and improvement of convergence, Phys. Rev. Fluids **4**, 084104 (2019).
[77] J. Ainley, S. Durkin, R. Embid, P. Boindala, and R. Cortez, The method of images for regularized Stokeslets, J. Comput. Phys. **227**, 4600 (2008).
[78] R. Cortez and D. Varela, A general system of images for regularized Stokeslets and other elements near a plane wall, J. Comput. Phys. **285**, 41 (2015).
[79] M. W. Rostami and S. D. Olson, Fast algorithms for large dense matrices with applications to biofluids, J. Comput. Phys. **394**, 364 (2019).
[80] W. Yan and R. Blackwell, Kernel aggregated fast multipole method, Adv. Comput. Math. **47**, 69 (2021).